

Probing Wolf-Rayet Winds: *Chandra*/HETG X-Ray Spectra of WR 6

David P. Huenemoerder^a, K. G. Gayley^b, W.-R. Hamann^c, R. Ignace^d, J. S. Nichols^e,
L. Oskinova^c, A. M. T. Pollock^{f,g}, N. S. Schulz^a, T. Shenar^c

ABSTRACT

With a deep *Chandra*/HETGS exposure of WR 6, we have resolved emission lines whose profiles show that the X-rays originate from a uniformly expanding spherical wind of high X-ray-continuum optical depth. The presence of strong helium-like forbidden lines places the source of X-ray emission at tens to hundreds of stellar radii from the photosphere. Variability was present in X-rays and simultaneous optical photometry, but neither were correlated with the known period of the system or with each other. An enhanced abundance of sodium revealed nuclear processed material, a quantity related to the evolutionary state of the star. The characterization of the extent and nature of the hot plasma in WR 6 will help to pave the way to a more fundamental theoretical understanding of the winds and evolution of massive stars.

Subject headings: stars: Wolf-Rayet — stars: massive — stars: individual (WR 6) — X-rays: stars

^aMassachusetts Institute of Technology, Kavli Institute for Astrophysics and Space Research, 70 Vassar St., Cambridge, MA, 02139, USA (dph@space.mit.edu)

^bDepartment of Physics and Astronomy, University of Iowa, Iowa City, IA 52242, USA (ken.gayley@gmail.com)

^cInstitut für Physik und Astronomie, Universität Potsdam, Karl-Liebknecht-Str. 24/25, D-14476 Potsdam, Germany (wrh@astro.physik.uni-potsdam.de, lida@astro.physik.uni-potsdam.de, shtomer@astro.physik.uni-potsdam.de)

^dDepartment of Physics and Astronomy, East Tennessee State University, Johnson City, TN 37614, USA (ignace@mail.etsu.edu)

^eHarvard-Smithsonian Center for Astrophysics, 60 Garden St., MS 34, Cambridge, MA 02138, USA (jnichols@cfa.harvard.edu)

^fEuropean Space Agency, ESAC, Apartado 78, 28691 Villanueva de la Cañada, Spain

^gDepartment of Physics and Astronomy, Hounsfield Road, University of Sheffield, Sheffield S3 7RH, England

1. Introduction

Within the Wolf-Rayet (WR) class are some of the most massive and luminous of stars. Rapid outflow of their dense stellar winds enriches and energizes the interstellar medium before this brief phase culminates in a core-collapse supernova detonation (Langer 2012). The WR stars are thus important contributors to galactic feedback of nuclear-processed matter, mechanical energy, and ionizing radiation throughout cosmic history, greatly affecting their host star cluster as well as an entire galaxy. Characterization of WR star properties—especially mass-loss rate and composition—is usually done through optical and UV spectroscopy (Hamann, Gräfener & Liermann 2006; Hillier & Miller 1998). However, structure in highly supersonic winds will invariably lead to shocks and X-ray emission, so the X-ray regime is crucial for understanding the nature of the wind hydrodynamics, and the structures it produces. This also relates to the potential importance of magnetization in some winds. Such structures in hot-star winds can include embedded wind shocks, magnetic confinement in some cases, or wind-wind collisions in binary systems (Güdel & Nazé 2009). X-ray emission lines are key diagnostics of the high-energy processes, since line strengths and profile shapes provide detailed information about the wind structure and dynamics. There have been a large number of empirical and theoretical investigations of X-ray line fluxes and profiles since the advent of high-resolution spectroscopy with *Chandra* and *XMM-Newton*. Waldron & Cassinelli (2007) performed an empirical study of line characteristics in a collection of OB-stars. Hervé et al. (2012) examined theoretical profiles for emission distributed over a range of radii with different plasma conditions, while Leutenegger et al. (2006) investigated the effects of distributed emission specifically for He-like lines. Ignace & Gayley (2002) and Leutenegger et al. (2007) studied effects of resonant scattering on line profiles. Oskinova, Feldmeier & Hamann (2006) and Leutenegger et al. (2013) looked into effects of clumping or porosity on line shapes. Cohen et al. (2014b) did a systematic re-analysis of O-star line profiles to determine mass loss rates, Cohen et al. (2014a) applied an underlying shock cooling model to determine wind structure. Ignace (2015) has given a review of X-ray line profiles. This a highly selective and by no means exhaustive collection of X-ray emission line modeling and analysis work and indicates the importance and interest in this area.

The winds of hot stars are presumed to be accelerated by line-driven radiation pressure (Castor, Abbott & Klein 1975; Friend & Castor 1983; Pauldrach, Puls & Kudritzki 1986) which, due to instabilities, leads to soft X-ray (~ 0.2 keV) emitting shocks in the acceleration zone, typically well within a few stellar radii of the photosphere (Lucy & White 1980; Owocki, Castor & Rybicki 1988; Feldmeier, Puls & Pauldrach 1997; Krtićka et al. 2009). The rapid expansion leads to broad emission lines (MacFarlane et al. 1991; Ignace 2001; Owocki & Cohen 2001). The destruction of Helium-like forbidden line emission through intense photospheric UV photoexcitation provides a valuable diagnostic of the location of X-ray emission (Blumenthal, Drake & Tucker 1972; Waldron

& Cassinelli 2001; Kahn et al. 2001).

While the above scenario is quite successful in describing the general characteristics of OB-star X-ray emission, various details are still under intense debate, such as the minimum radius and extent of X-ray emission, the fraction of X-ray emitting plasma, and the clumpiness of the wind. There are cases, however, where this scenario is too simple, such as in magnetically confined wind shocks (Babel & Montmerle 1997; Gagné et al. 2005), which may have narrower lines and plasmas dominated by high temperatures (~ 2 keV), or in colliding wind binaries (Luo, McCray & Mac Low 1990; Stevens, Blondin & Pollock 1992; Parkin et al. 2014) which can have a range of temperatures and profiles, depending on the orbital separation and geometrical aspect (Henley, Stevens & Pittard 2003).

The massive winds of WR stars are also believed to host embedded shocks (Gayley & Owocki 1995) and should thus have some X-ray characteristics in common with O-stars. WR star winds, however, do have some significant differences from O-stars. Hydrogen is highly depleted or even absent. The mass loss rates are very high, so with similar wind velocities to O-stars of ~ 1000 km s⁻¹, WR stars have much denser winds, and given their enhanced metallicity, much higher X-ray continuum opacity. Metallicity has a very strong effect on the strength of WR star winds (Ignace & Oskinova 1999; Crowther & Hadfield 2006; Gräfener & Hamann 2008). Through the radiative losses of emission lines, metallicity will also affect the thermal structure of winds.

WR 6 (EZ CMa) has the spectral type WN 4, and is visually bright with a magnitude $V = 6.9$ (van der Hucht 2001), at a distance of 1.8 kpc (Howarth & Schmutz 1995). Its atmosphere and wind are dominated by helium, with no detectable trace of hydrogen (Hamann & Koesterke 1998b). A remarkable characteristic of WR 6 is that it has a well established and consistent photometric period of 3.7650 d determined from V , b , B , and narrow band photometry, as well as from spectrophotometry, though the modulation itself is highly variable in amplitude and phase (Georgiev et al. 1999; Robert et al. 1992; Lamontagne, Moffat & Lamarre 1986). The photometric amplitude has ranged from about 0.1 mag to unmodulated. The star is generally considered to be single, based on its radio and X-ray properties (Dougherty & Williams 2000; Oskinova 2005; Skinner et al. 2002a). Georgiev et al. (1999) argued for binarity based upon their determination that variations are coherent in phase over long times. Morel, St-Louis & Marchenko (1997), on the other hand, argued for a single star, with variability due to structure in the wind, since the variability sometimes vanishes. Skinner et al. (2002a) rejected the hypothesis of a compact companion, but they could not exclude the possibility of a low-mass pre-main-sequence companion, though they concluded that without direct evidence, the star should continue to be considered single. Hence, for the present purposes, we will consider WR 6 to be single.

WR 6 has no detected global magnetic field (de la Chevrotière et al. 2013), and so is not suspected of having a magnetically confined wind.

Table 1 WR 6 Basic Properties

| Property | Value |
|-------------------------------------|---------------------------------|
| Spectral Type | WN4 |
| R_*/R_\odot | 2.65 ^a |
| T_* [kK] | 89 ^a |
| $M [M_\odot]$ | 19 ^a |
| $\log(L_{\text{bol}}/L_\odot)$ | 5.6 ^a |
| v_∞ [km s ⁻¹] | 1700 ^a |
| | 1950(20) ^b |
| $\dot{M} [M_\odot \text{ yr}^{-1}]$ | 5×10^{-5} ^a |
| d [kpc] | 1.82 ^c |
| Epoch [JD] | 2 443 199.53 ^d |
| Period [day] | 3.7650 ^d |

^aHamann, Gräfener & Liermann (2006)

^bThis work (1σ uncertainty in parenthesis.)

^cHowarth & Schmutz (1995)

^dGeorgiev et al. (1999)

Some fundamental parameters of WR 6 are given in Table 1, many from the comprehensive modeling of galactic WN stars by Hamann, Gräfener & Liermann (2006), or as updated in this work.

The first high-resolution X-ray spectrum of WR 6, obtained with the *XMM-Newton* Reflection Grating Spectrometer (RGS), showed that the X-rays from this star are generated by a new and unknown mechanism, different from O-star winds (Oskinova et al. 2012) in that the X-rays do not appear to be consistent with O-star embedded wind shocks (Krtićka et al. 2009), or with magnetic confinement close to the star. The hot, X-ray emitting plasma of WR 6 exists far out in the wind, as determined from He-like line ratios and also from the presence of Fe K fluorescence, likely produced from cool wind plasma illuminated by hard X-rays. New mechanisms are required to explain this emission. This fascinating situation demonstrates that we do not fully understand some important aspects of the winds of massive stars in the crucial evolutionary stages immediately prior to a supernova explosion.

The wind-broadened line profiles in WR 6 were only marginally resolved by the *XMM-Newton* RGS. Therefore we obtained Chandra spectra using the High Energy Transmission Grating Spectrometer (HETGS) which provides significantly superior spectral resolving power, being four times better than that of the RGS. The HETGS pass-band covers the strategic lines of S, Si, Mg, and Ne, which are needed to understand the distribution of the hottest gas in the WR wind—He-like ratios reveal the radial location, H-to-He-like ratios specify temperatures, and line positions and profile widths reveal the wind dynamics. Therefore, we used HETGS to study this mystery uncovered by *XMM-Newton*. Figure 1 gives an overview of the important part of the spectrum observable with HETGS.

2. Observations and Calibration

Using the *Chandra*/HETG spectrometer (Canizares et al. 2005), we observed WR 6 three times in 2013 for a total of 440 ks. Dataset identifiers and exposure times are given in Table 2. The HETGS spectra cover the range from about 1–30 Å, as dispersed by two types of grating facets, the High Energy Grating (HEG) and the Medium Energy Grating (MEG), with resolving powers ranging from 100 to 1000, with approximately constant full-width-half-maxima (*FWHM*) of 12 mÅ for HEG and 23 mÅ for MEG.

The *Chandra* data were reprocessed with standard Chandra Interactive Analysis of Observations (CIAO) programs (Fruscione et al. 2006) to apply the most recent calibration data (CIAO 4.6 and the corresponding calibration database, version 4.5.9). The counts spectra are thus composed of 4 orders per source per observation: the positive and negative first orders for each grating type,

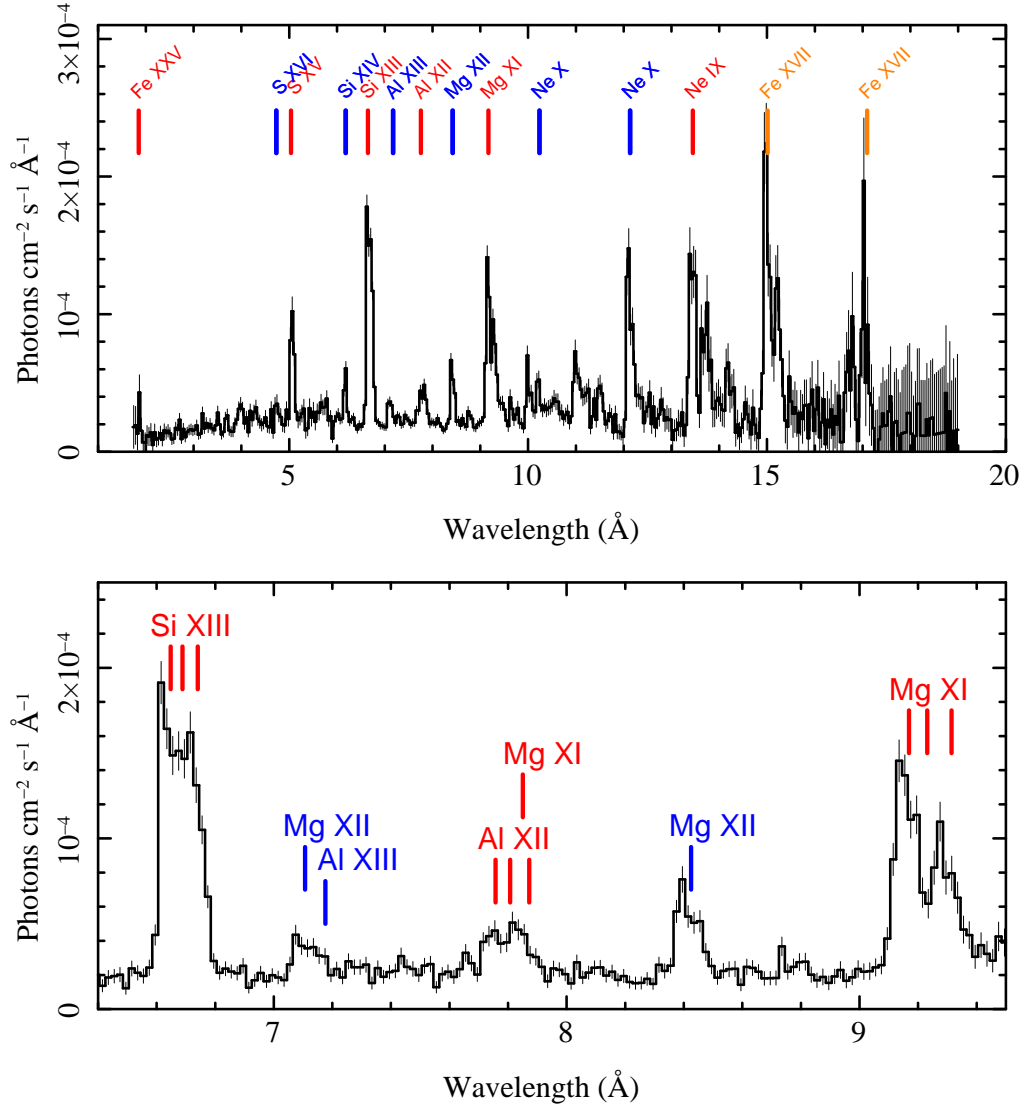


Fig. 1.— The HETGS spectrum of WR 6: combined HEG and MEG first orders, in flux units. The locations of some spectral features, primarily H- and He-like ions, are marked. The top panel shows the useful range of the instrument, with bins of 0.04 Å (2 MEG, 8 HEG resolutions elements). The bottom panel shows detail, including the resonance, intercombination, and forbidden line locations (short-to-long wavelength) for a narrow region, binned to 0.04 Å. Line labels are blue for H-like ions, red for He-like, and orange for others. Error bars are 1σ .

the MEG and HEG, which have different efficiencies and resolving powers. The default binning over-samples the instrumental resolution by about a factor of 4.

Several calibration files are required for analysis to convolve a model flux spectrum with the

instrumental response in order to produce model counts. These are made for each observation and each spectral order by the CIAO programs which use observation-specific data in conjunction with the calibration files to make the effective area files (“Auxiliary Response File”, or ARF) and the spectral redistribution and extraction-aperture efficiency files (“Response Matrix File”, or RMF) (Davis 2001).

Since emission lines in the WR 6 spectrum are broad and well sampled at the lower MEG resolution, during analysis we regridded the HEG spectra and response matrices onto the MEG grid so that the spectra could be combined. This primarily aids visualization of the data as one spectrum.

Figure 1 shows the combined photon flux spectrum¹ for the HEG and MEG first orders. Some prominent features are marked, mainly the H-like and He-like lines of abundant chemical elements, and some strong Fe lines. Due to the low effective area beyond about 20 Å, the interstellar medium (ISM) absorption on the line-of-sight, wind absorption (intrinsic to WR 6), and the absence of oxygen in the atmosphere, there is little signal detected by the HETGS at the longer wavelengths. The ISM component has a transmission factor of 0.95 at 5 Å, but ~ 0.2 at 20 Å. The wind-local absorption has a slightly larger effect, with a combined ISM/wind result of about 50% transmission at 10 Å, but only 3% at 20 Å. (The wind-local model of emission and absorption is discussed in more detail in Section 3 and Appendix A.1.)

The zeroth order is useful for measuring the Fe XXV line, constraining the hottest plasmas present, and for variability studies, since the CCD photon pileup being fairly small at a rate per frame of less than 0.1 counts s⁻¹. We show this region of the zeroth order spectrum in Figure 2.

3. Spectral Modeling

The X-ray emission line strengths and profiles from stellar winds are very sensitive to the wind structure and dynamics. MacFarlane et al. (1991) showed that the profile from a geometrically thin shell ranges from a flat-topped profile of width determined by the expansion velocity, to a triangular profile if the foreground wind shell’s continuum opacity obscures the receding shell. Ignace (2001) studied the line profile for a shell undergoing constant spherical expansion, including the limit of high continuum opacity. Owocki & Cohen (2001) extended the formalism to a radially-dependent expansion velocity with arbitrary continuum opacity and showed that profiles are generally asymmetric, with a blue-shifted centroid, again due to absorption of the receding wind by the intervening wind. They also modeled the effect of a minimum radius of line forma-

¹Flux calibration is described in Appendix A.2.

Table 2 Observational Information

| Date ^a | ObsID ^b | Exp [ks] | $\langle Rate \rangle^c$ [cts ks ⁻¹] |
|--|--------------------|-------------|---|
| 2013-05-03T04:34:39 | 14534 | 168 | 51.2 (0.6) |
| 2013-08-15T08:22:51 | 14535 | 97 | 55.7 (0.8) |
| 2013-08-19T13:45:08 | 14533 | 175 | 57.9 (0.6) |
| Total exposure [ks] | | 440 | |
| Count rate (diffracted) ^c [cts ks ⁻¹] | | 32.8 | |
| Count rate (direct) ^c [cts ks ⁻¹] | | 22.4 | |

^aThe date of observation is given by the FITS standard CCYY-MM-DDThh:mm:ss.sss, which is the universal time at the start of the exposure, as encoded into the FITS file header keyword DATE-OBS.

^bThe *Chandra* observation identifier.

^cThe mean count rate is given for each ObsID for the combined first and zeroth orders, with the one standard deviation error of the mean in parentheses. The diffracted count rate is for photons in the first orders of HEG and MEG. The direct rate is for photons in the zeroth order.

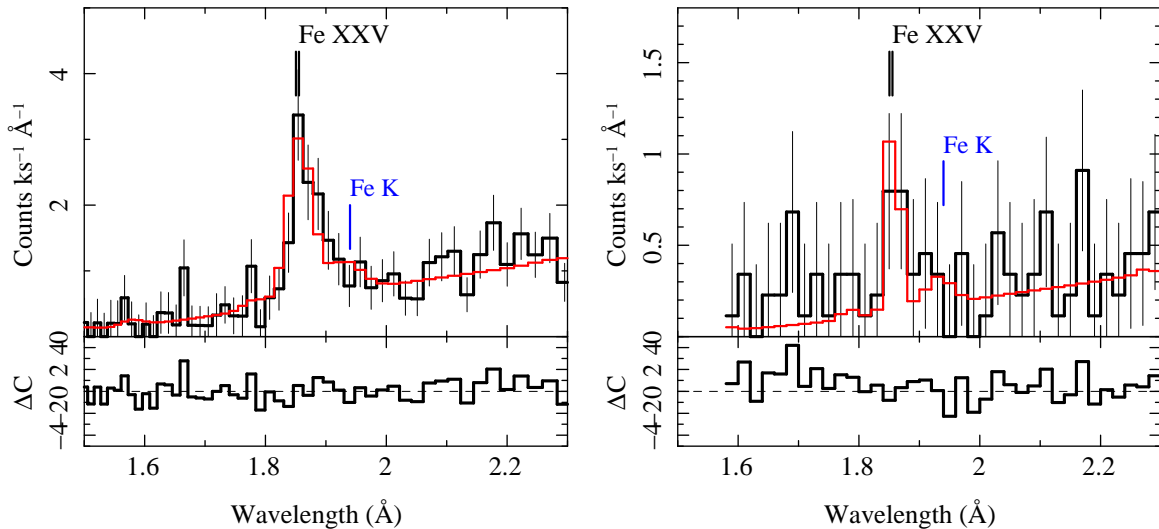


Fig. 2.— The HETGS zeroth order spectrum of WR 6 (left) and the dispersed spectrum (right) in the Fe K region. The strong emission line is the blend of He-like resonance, intercombination, and forbidden lines of Fe XXV (1.85 \AA , 6.70 keV) having peak emissivity near 60 MK . The model shown in red is an isothermal APEC model with $T = 43 \text{ MK}$. A fit of an Fe K fluorescent feature at 1.94 \AA (6.39 keV) is consistent with the *XMM-Newton*-determined value (Oskinova et al. 2012), though is of very low significance in these data, changing the statistic from 1.12 to 1.04. Error bars are 1σ .

tion, showing how a central void (in both velocity and emission measure) can strongly affect the line profile by flattening the peak, since the volume of higher density, low-velocity plasma has been reduced. Oskinova, Feldmeier & Hamann (2004, 2006) showed how clumping in the wind can affect the emergent profile, and, depending on clumping parameters, result in unshifted, symmetric profiles, in contrast to a smooth wind’s skewed profiles.

The *XMM-Newton*/RGS spectra showed that the X-ray line profiles of WR 6 are broadened by an amount consistent with $v_\infty = 1700 \text{ km s}^{-1}$, and that a blueshifted Gaussian profile with $\Delta v \approx -650 \text{ km s}^{-1}$ generally gave an adequate fit (Oskinova et al. 2012). With the higher resolution of HETG, we find that a Gaussian is a very poor approximation to the profile. Instead, we find that a spherical constant velocity expansion model, similar to that described by Ignace (2001), gives a very good fit.

As a baseline for modeling the lines, we assumed a provisional plasma model based on the RGS analysis of Oskinova et al. (2012). This is primarily a phenomenological model because it does not entail distributed emission and absorption throughout the wind, but is a slab model, with an underlying multi-thermal plasma, overlying wind absorption with ionized wind edges, and an interstellar foreground absorption component. This serves as a basis for identifying and charac-

terizing spectral features, and incorporates blends from the basic plasma model. We extended the 3-temperature APEC (Smith et al. 2001; Foster et al. 2012) model used in the RGS analysis by including an additional temperature component to satisfy the higher energy response of HETG, and we re-fit the temperatures and normalizations simultaneously for HETG’s first and zeroth orders, *XMM-Newton* RGS-1 and -2 first and second orders, and the *XMM-Newton* EPIC MOS and PN spectra. Absorption components, which were determined from *XMM-Newton* analysis, were left fixed, since they are better constrained by the longer wavelength data. A model summary is given in Table 3, and more details are given in Appendix A.1.

3.1. Line Profile Modeling

The lines are well resolved by HETG and are very non-Gaussian. They are fin-shaped, with a sharp blue edge, upward-convex, sloping down to the red. Figure 1 (bottom panel) shows detail for a narrow spectral region and demonstrates the near-vertical blue edge and maximum being blueward of line center. The profiles are very much like those shown in Ignace (2001), or of the profiles from optically thick (in the continuum) winds with a large central cavity (e.g. Owocki & Cohen 2001, see their Figure 2).

For WR winds it is natural to expect line profiles that sample the asymptotic flow, because the winds are quite dense such that optical depth unity in photoabsorption of X-ray emission is expected to be at relatively large radius. The analytic solutions of Ignace (2001) were developed for just this case.

We have adopted the analytic form of Ignace (2001) for the line profile, $f(w_z)$, valid in the limit of large optical depth:

$$f(w_z) = f_0 \left[\frac{\sqrt{1 - w_z^2}}{\arccos(-w_z)} \right]^{1+q} \quad (1)$$

where f_0 is a normalization constant, and w_z is the dimensionless scaled velocity along the line-of-sight z , $w_z = (c/v_\infty)(\lambda/\lambda_0 - 1)$ for a line having rest wavelength λ_0 . In this formula the emissivity per volume is assumed to vary as the square of density. However, an additional modification to the emissivity is allowed in the form of r^{-q} , with $q > -1$ as outlined in Ignace (2001, see Equation 8 and associated discussion therein). This q parameter serves to modify the shape of the line profile from a pure density squared result. Physically, one can think of this accompaniment to the line emissivity as representing perhaps a number of factors, including a volume filling factor to accommodate clumping, or a radius-dependent X-ray temperature distribution to accommodate variations in shock strength. In this sense different q values are to be expected from fits to different lines, in contrast to seeking a single value of q that applies to all lines.

As an illustration, a family of model line profiles are shown in Figure 3 for a range of q values. Note that the photoabsorption optical depth is assumed large, meaning that X-rays from near the stellar photosphere are strongly absorbed, and that the X-ray line profile is formed generally in the vicinity of optical depth unity in photoabsorption, although this depends in detail on the value of q . As seen in Figure 3, the case of $q = 0$ gives the canonical “fin”-shaped line profile. Positive values of q serve to exacerbate the relative sharpness of the fin; negative values of q reduce, to the extreme that $q = -1$ recovers a “flat-top” line profile that is normally associated with the case of zero photoabsorption.

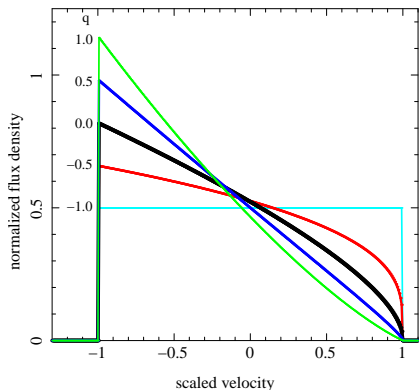


Fig. 3.— Example intrinsic line profiles for constant spherical expansion for several values of q , as defined by Equation 1.

In using the adopted form of Equation 1 to model line profiles, we have made several assumptions. First, that the X-ray line emission is taken to be well-described by collisional ionization equilibrium in which every collisional excitation is from the ground state and results in a radiative transition, with negligible optical depth in the lines. This serves as the basis of the density-squared emissivity. Second, the continuum opacity of the WR 6 wind is very large. In soft X-rays, the large radial optical depth prevents us from seeing down to the acceleration zone, so constant expansion is a reasonable assumption for the visible plasma. In this limit, if we assume that all X-ray emission lines have the same profile, then it means they all sample the same terminal velocity with the same temperature (or same temperature distribution).

To relax the latter assumption, that all lines have a common thermal origin with similar hot-gas filling factor, we allow the exponent, q , to be non-zero. In this way, we can fit individual profiles to explore trends in expansion velocity or shape. For example, the continuum opacity is lower at shorter wavelengths; if it is significantly smaller such that we can see deeper, where conditions may be different, we might expect the shortest wavelength lines to have a different shape from the longer wavelength lines even though all the lines form in the asymptotic terminal speed flow.

We have implemented the model line profile as a parametric fit function, but also as a global

intrinsic line profile in the APEC model evaluation (that is, our APEC model, in addition to the usual parameters of temperatures, normalizations, abundances, and Doppler shift, has wind-profile parameters). To determine the profile parameters (since the global plasma model is not necessarily the best model for all features), we independently fit narrow spectral regions containing strong or important lines by adopting the 4-temperature model as a starting point and then fit the normalization, relevant elemental abundances (to allow optimization of the line-to-continuum ratios), and—of primary interest—wind parameters q and v_∞ . We adopted line-of-sight Doppler velocity of 46.2 km s^{-1} , which is the exposure-time weighted mean of the systemic (Firmani et al. 1980) plus line-of-sight velocities for the three observations, which ranged from $34\text{--}66 \text{ km s}^{-1}$. The differences between the observations are negligible in consideration of the resolution and the line width, though very important to set a priori because the terminal velocity and Doppler shift are degenerate parameters. We take the Doppler velocity as a given, and do not fit the line center.

One must be careful to distinguish the line *center* from a line *centroid*. A common diagnostic of stellar winds is often referred to as a “blueshifted profile”. This is incorrect when referring to the volume-integrated profile: the *centroid* is blueward of line center because the wind opacity causes the emergent profile (centered at zero velocity) to be skewed through absorption of locally redshifted wind emission. Here we specifically refer to the theoretical line profiles’ centers when we indicate the line position.

In Figure 4, we show observed and model profiles for relatively clean portions of the spectrum, to demonstrate the “fin”-shape and relative position of the line center. The models were APEC plasmas fit within the narrow regions as described above.

For the He-like lines, we also used density as a free parameter to allow the important forbidden (f) to intercombination (i) line flux ratio ($R = f/i$) to be free; use of density is simply a convenient proxy for consideration of UV photoexcitation from the forbidden to intercombination levels (Blumenthal, Drake & Tucker 1972). The density dependence was computed with APEC, then parameterized for use as a line emissivity modifier.² As an alternative, we also fit the He-like lines parametrically using a linear combination of a continuum and line components. This is less physically constrained than the plasma-model approach since, for instance, there is no a priori relation between the forbidden and intercombination line. Uncertainties in this approach tend to be large because the lower limit on the intercombination line can be very small, and the forbidden-to-intercombination ratio arbitrarily large; hence we favor the APEC-based results. The fitted values are given in Table 4.

We show as an example the fit to the Si XIII lines in Figure 5, as well as the decomposition into the component profiles. The lines are well resolved. One discrepancy for Si XIII is a relatively large

²See http://space.mit.edu/cxc/analysis/he_modifier for details, data, and code.

Table 3 Model Parameters

| Property | Value |
|--|-------------------|
| Temperatures, T_x [MK] | 1.5, 4.0, 8.0, 50 |
| Normalizations [relative] | 10, 3.3, 1.9, 0.9 |
| $\log f_x$ [erg cm ⁻² s ⁻¹] | -11.9 |
| $\log L_x$ [erg s ⁻¹] | 32.9 |
| $\log(L_x/L_{\text{bol}})$ | -6.3 |
| $\log N_{\text{H}}$ [cm ⁻²] ^a | 21.2 |

^aForeground interstellar absorption. Flux is as-observed, whereas luminosity has been corrected for foreground interstellar absorption.

Table 4 R Values for He-like Lines

| Ion | λ Å | R f/i | R_0 $\max(f/i)$ |
|---------|----------------|-------------------|----------------------|
| S XV | 5.04 | 1.85 (0.50, 1.85) | 1.85 |
| Si XIII | 6.65 | 2.41 (2.19, 2.41) | 2.41 |
| Mg XI | 9.17 | 2.95 (2.32, 2.95) | 2.96 |
| Ne IX | 13.45 | 3.35 (2.29, 3.35) | 3.35 |

Note. — Limits for 90% confidence intervals are given in parentheses. Wavelengths are given for the resonance lines. R_0 is for the 4-temperature model, and so may differ slightly from the value at the temperature of maximum emissivity for each ion.

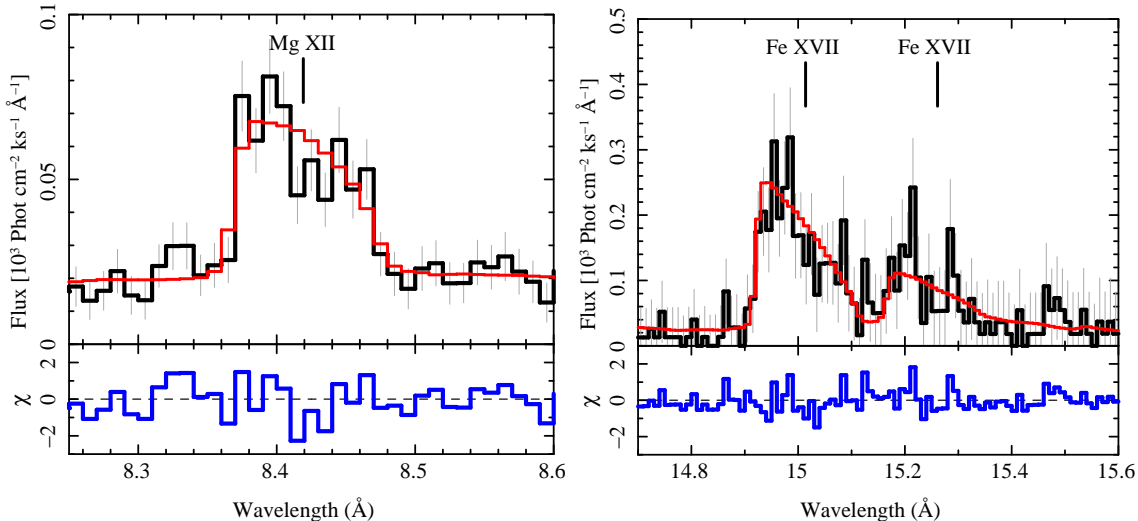


Fig. 4.— The fits to Mg XII (left) and Fe XVII (right), which shows the data (black) and model profile (red) for some relatively unblended features to demonstrate the “fin” shape of the lines. The line centers of the strongest lines in the region are marked; other model lines in the regions shown are an order of magnitude fainter than the brightest. The lower panels show the fit residuals.

feature in the residuals, which might mean that the i -component is narrower than the others (all three components shared the same profile parameters in the fit, as shown in Figure 7 and Table 5).

In Figure 6 we show a broader region of the spectrum along with the same spectral region as observed with RGS (bottom panel pair). This clearly demonstrates the character of the profiles’ vertical blue edge and the great advantage of the HETG’s higher resolution for determining the profile shape. With RGS, we could determine that the lines are broad, but a near-Gaussian profile was sufficient to fit them.

From fitting the narrow spectral regions with the APEC-based model including the model line profile of Equation 1, we have determined an error-weighted-mean expansion velocity of $1950 \pm 20 \text{ km s}^{-1}$, somewhat larger than the average value of 1700 km s^{-1} as determined by (Hamann, Gräfener & Liermann 2006) from analysis of the full spectrum, but smaller than the maximum value of $2100\text{--}2500 \text{ km s}^{-1}$ as observed among the UV lines in the several hundred archived IUE spectra. Our result is dominated by the best-determined value for Si XIII. A straight mean and standard deviation gives $1880 \pm 140 \text{ km s}^{-1}$. The lines are all consistent with a shape parameter of $q \simeq -0.2$ (Ignace 2001), which is close to zero, the nominal value for density-squared emissivity and uniform expansion (see Equation 1 and Figure 3). We show the determinations for each feature measured in Figure 7, and the values are listed in Table 5.

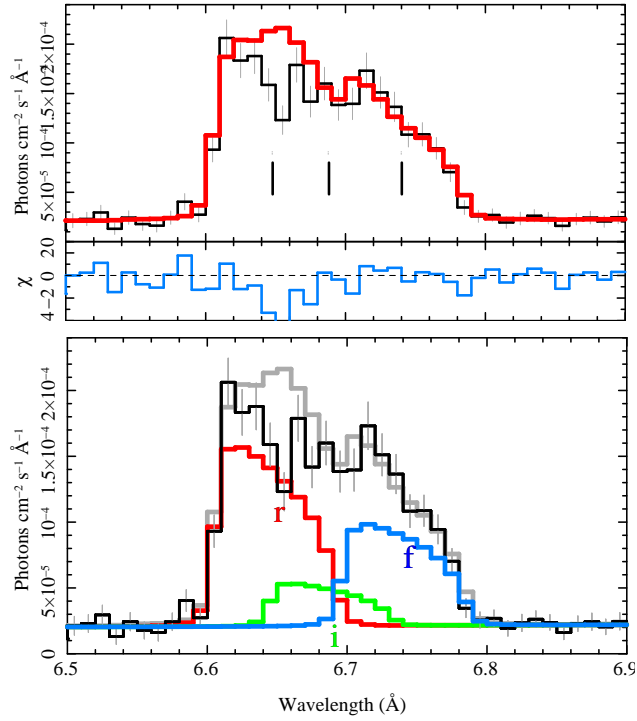


Fig. 5.— The fit to Si XIII. The top panel shows the photon flux spectrum (black), the model (red) and the residuals below in the small sub-panel. The bottom plot shows the same counts (black) and model (gray), but also shows the components for the resonance (red), intercombination (green), and forbidden (blue) lines (also labeled as *r*, *i*, and *f*). Line centers (*not centroids*) are marked in the upper panel. The three model components shown do not sum to the total, which includes additional flux from many dielectronic recombination lines, as well as a small contribution from Mg XII.

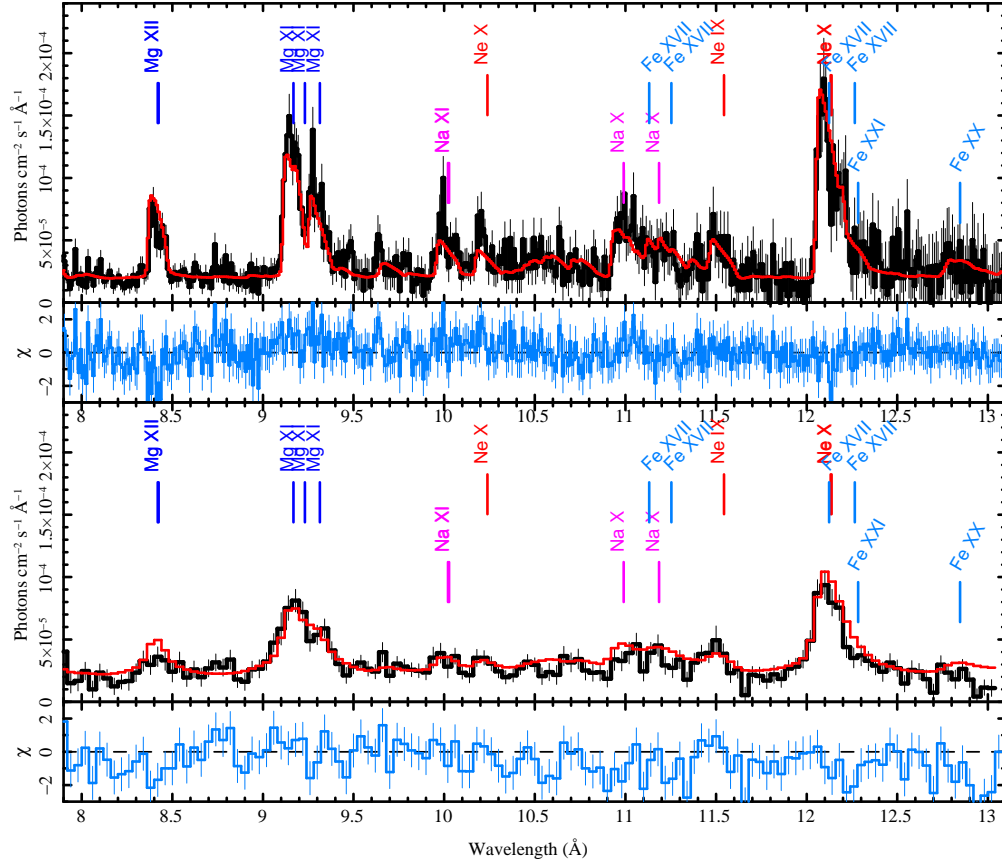


Fig. 6.— Here we compare the model to the photon flux HETG spectrum (top), and the same model to the RGS spectrum. In each case, the black histogram is the observed spectrum with two bins per resolution element, and the red is the model. Below each are the residuals. In this region it is clear that the HETG has resolved the sharp blue edges on the profiles, which were not evident in the lower-resolution RGS data.

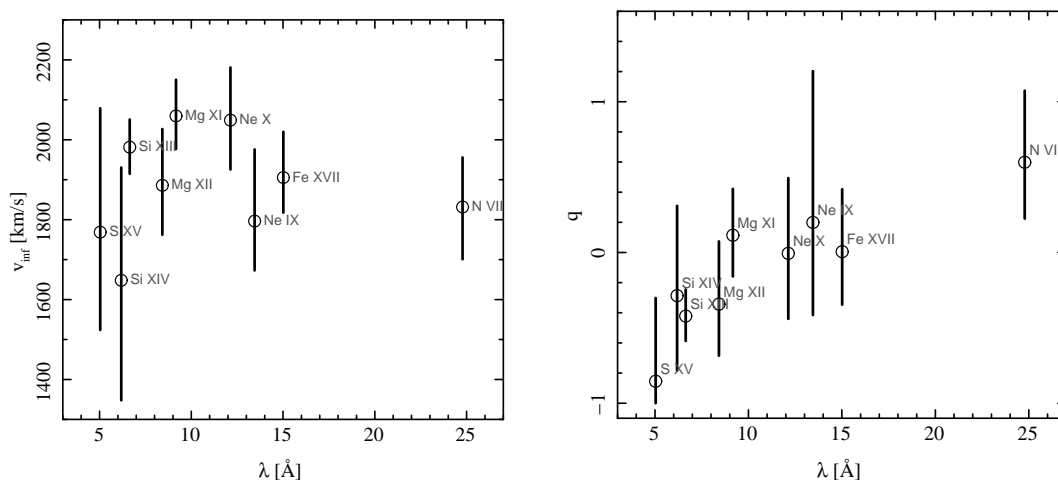


Fig. 7.— The line width and shape parameters against wavelength. On the left, there is no apparent trend of width with wavelength. On the right, there is a weak trend in the shape with wavelength. Errorbars give 90% confidence intervals. The points for N VII are from *XMM-Newton*/RGS data.

Table 5 Line Shape Parameters

| Line | λ [\AA] | v_{∞} [km s^{-1}] | q |
|---------|-------------------------------|--|----------------------|
| S XV | 5.04 | 1770 (1520, 2080) | -0.86 (-1.00, -0.30) |
| Si XIV | 6.18 | 1650 (1350, 1930) | -0.29 (-0.78, 0.31) |
| Si XIII | 6.65 | 1980 (1920, 2050) | -0.42 (-0.59, -0.25) |
| Mg XII | 8.42 | 1890 (1760, 2030) | -0.34 (-0.68, 0.07) |
| Mg XI | 9.17 | 2060 (1980, 2150) | 0.11 (-0.16, 0.42) |
| Ne X | 12.13 | 2050 (1930, 2180) | -0.01 (-0.44, 0.49) |
| Ne IX | 13.45 | 1800 (1670, 1980) | 0.20 (-0.42, 1.20) |
| Fe XVII | 15.01 | 1900 (1820, 2020) | 0.00 (-0.35, 0.42) |
| N VII | 24.78 | 1830 (1700, 1960) | 0.60 (0.22, 1.07) |

Note. — The 90% confidence limits are given in the parentheses. The values for N VII are from *XMM-Newton*/RGS data.

3.2. Light Curve Extraction

To examine the time history of the X-ray emission, we binned count-rate light curves from both the dispersed and zeroth order events. For dispersed events, we used the program, `aglc`³ which handles the dispersed photon coordinates and CCD exposure frames over multiple CCD chips. We used first order photons from both HEG and MEG gratings over the range 1.7–17.0 Å. For zeroth order curves, which involve only one CCD chip, we used the CIAO program, `dmextract`. Count rates from the dispersed spectrum were slightly higher than from zeroth order. Figure 8 shows the combined zeroth and first order rates for each of the three observations. Table 2 lists the mean count rates per observation and the overall means for dispersed and zeroth orders. Hardness ratios were also computed, but since these showed no trend, we have not included them in the figure.

Optical photometry was obtained with the *Chandra* Aspect Camera Assembly (ACA) simultaneously with the X-ray data. This camera has an approximately flat broadband response between 4000-8000Å. Details of this system as used for studying stellar variability can be found in the “*Chandra* Variable Guide Star Catalog”⁴ (*VGuide*; Nichols et al. 2010). Empirical uncertainties were estimated from the variance in flat portions of *VGuide* light curves for several stars over a range of magnitudes. The optical light curve, obtained during the *Chandra* observations, is shown in Figure 8.

4. Discussion

4.1. Line Shapes and Ratios

The line profiles of WR 6 are indicative of a constant spherical expansion. All the lines in the HETGS range have similar shape and width. This implies that the radiation in all lines likely suffers from equally strong wind absorption, and that for each line we see only radiation originating from a flow with similar velocity ranges. In the relatively thin-wind OB-stars, there is a strong correlation between the line width and the wavelength. Since the continuum opacity is proportional to wavelength, shorter wavelength lines are formed deeper in the wind where the expansion velocity is smaller. In stars like ζ Oph or δ Ori, there is a trend of a factor of two or more in line widths over the HETGS bandpass (Cassinelli et al. 2001; Nichols & et. al 2015). Furthermore, the line shape is strongly affected by material over a broad range of velocities, and

³ACIS Grating Light Curve, or `aglc`, is available from <http://space.mit.edu/cxc/analysis/aglc/>

⁴<http://cxc.harvard.edu/vguide/>

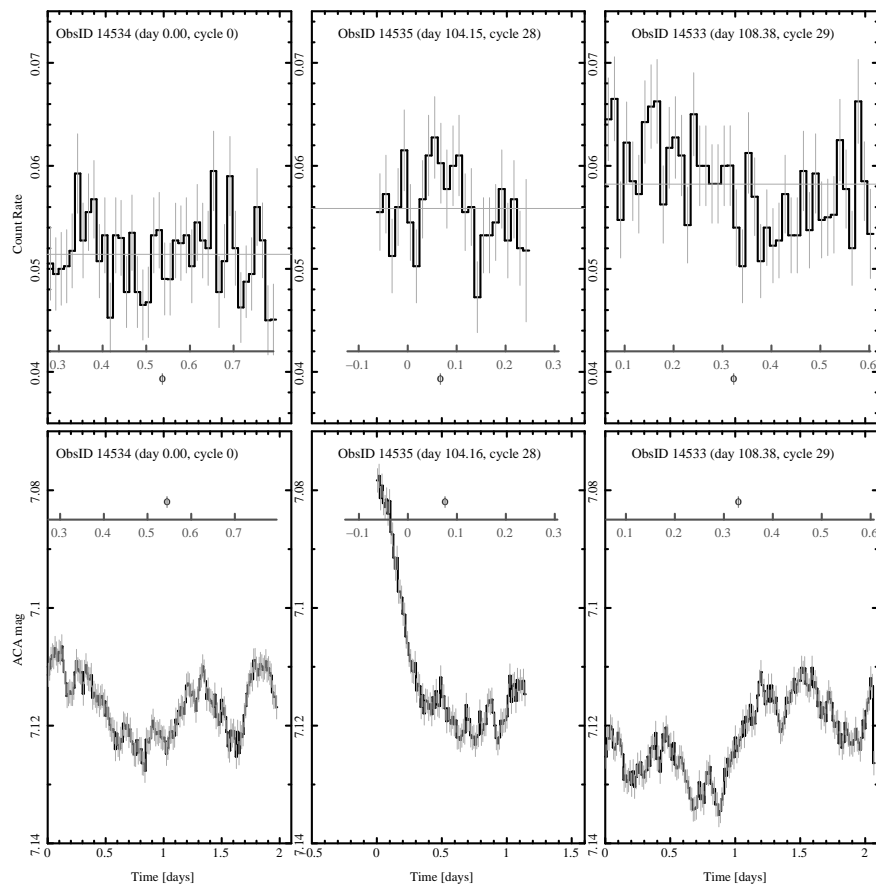


Fig. 8.— Light curves; Top: HETG dispersed first order plus zeroth order light curve for each observation as labeled. The “day” value is the number of days since the Time = 0 point, based on the first observation, in each panel, and the cycle is the number of periods since the $\phi = 0$ occurrence immediately preceding the start of the first observation. The inset axis gives the phase according to the ephemeris of Georgiev et al. (1999, (see Table 1)). The bin size is about 4 ks, and errorbars are 1σ . The horizontal gray line is the mean count rate for the observation. Bottom: the *CXO* aspect camera (ACA) broad-band optical light curves in 1 ks bins taken simultaneously with the X-ray observations. We have plotted 2σ uncertainties, estimated to be about 0.002 mag in the 1 ks bins, based on other (but flat) light curves at similar magnitude in the *Chandra* Variable Guide Star Catalog (Nichols et al. 2010). See Table 2 for observation dates.

in some cases, there is evidence of temperature stratification (Hervé, Rauw & Nazé 2013). In Figure 7 we see little or no trend in the line width with wavelength, and perhaps a weak trend in the shape. Hence, the evidence is strong that even down to Si and S (5–7 Å, or to 2.5 keV), we are only seeing X-ray emission from large radii. Recall that for no photoabsorption, $q = -1$ and a flat-topped profile would result. The weak trend in q with wavelength in Figure 7 is consistent

with seeing more emitting volume at shorter wavelengths, where the continuum opacity is lower. However, it will take higher sensitivity to determine if this trend is real. It will be very interesting when high resolution profiles can be obtained in Fe XXV (such as with *Astro-H*) where we expect to be able to see to below $\sim 10 R_*$, to determine whether q is indeed smaller, and also to see if the line is narrower, since at those radii we expect the wind velocity to be below about $\sim 75\%$ of the terminal velocity.

The strong UV radiation emerging from the star affects the observed f/i ratios of He-like ions, which otherwise depend solely on the temperature of the hot plasma. By using the stellar UV field as an input, the observed f/i ratios can be used to trace the formation region of these lines (Gabriel & Jordan 1969; Porquet et al. 2001; Waldron & Cassinelli 2007). A detailed treatment allows one to construct an equation which predicts the f/i line ratio \mathcal{R} as a function of the radiative excitation rate ϕ_ν and the electron density n_e (cf. Blumenthal, Drake & Tucker 1972, Eq. 1c). In the case of hot stars, the contribution of n_e is almost always negligible compared to that of ϕ_ν (see e.g. Shenar et al. 2015a,b). The simplest approach for estimating the formation region would be to assume that the X-ray emitting gas is sharply located at a certain radial layer, which we refer to as the formation radius. It is more likely, however, that the X-rays originate over an extended region. In this case, one can derive the minimal radius where the X-ray emission of the concerned lines is originating, referred to as the onset radius. This involves the integration of the X-ray radiation emanating from a continuous range of radii, a method described by Leutenegger et al. (2006), and here extended to include the effect of K-shell absorption in the cold wind (Shenar et al. in preparation).

To determine the UV excitation rate ϕ_ν and the cold wind opacity κ_ν , we calculated a model for WR 6 using the non-LTE Potsdam Wolf-Rayet (PoWR) code (Hamann & Gräfener 2004) with the parameters listed in Table 4 as input (also shown in Figure 9). The PoWR code solves the non-LTE radiative transfer in a spherically expanding atmosphere simultaneously with the statistical equilibrium equations, while accounting for energy conservation. Complex model atoms with hundreds of levels and thousands of transitions are taken into account, along with millions of iron and iron-group lines which are handled using superlevels (Gräfener, Koesterke & Hamann 2002). The PoWR models account for stellar wind clumping in the standard volume filling factor micro-clumping approach (e.g. Hamann & Koesterke 1998a), or with an approximate correction for wind clumps of arbitrary optical depth (macro-clumping, Oskinova, Hamann & Feldmeier 2007). The X-ray emission and its effects on the ionization structure of the wind is included in the PoWR atmosphere models according to the recipe of Baum et al. (1992). The absorption of the X-ray radiation by the relatively cool (non-X-ray emitting) stellar wind is taken into account, as well as its effect on the ionization stratification by the Auger process. The contributions of diffuse emission from the stellar wind and of limb darkening are accounted for, and the mean intensity is accurately calculated in the reference frame of the wind. For the He-like lines, the constants R_0

and ϕ_c per ion, which are calculated at a temperature at which the X-ray emission of the ion in question peaks, are adopted from Leutenegger et al. (2006).

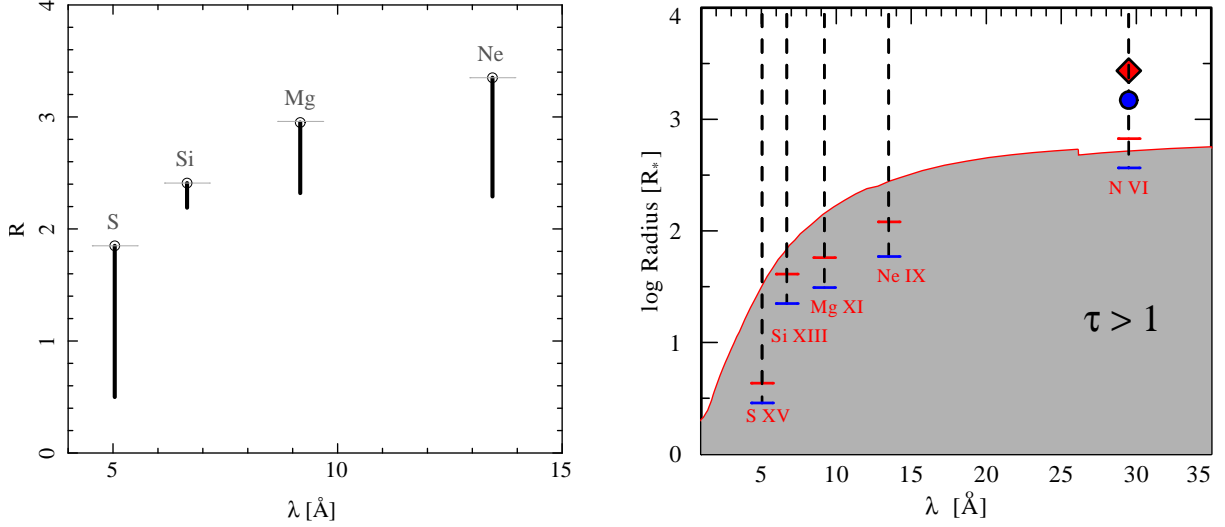


Fig. 9.— Left: the He-like R -ratios. The circles show the best fit values, and the errorbars are 90% confidence limits. Horizontal gray segments show the maximum R for the adopted multithermal model. Right: Using the plasma model R fits, we show the lower limits for the He-like inferred radii of X-ray emission onset for distributed emission (lower, or blue bars) or alternatively, of formation in the localized assumption (red, or upper bars), versus the line wavelengths. N VI is the only ion for which a formation radius (red diamond) and an onset radius (blue circle) could be established (using measurements from XMM-Newton observations). The gray region shows where the continuum opacity has $\tau_\lambda \geq 1$, according to the wind model.

The right panel of Figure 9 graphically summarizes our results for the He-like ions S XV, Si XIII, Mg XI and Ne IX. The red bars (upper of the pair) depict the derived 90% confidence lower limit formation radius for each He-like ion, assuming a localized formation region. The blue bars (lower of the pair) similarly depict the onset radii, assuming an extended formation region. (These correspond to the lower limits of the R ratios as shown in the left-hand panel of Figure 9; the best fit values yield large, unconstrained upper radii, except for N VI). At radii within the gray area, the wind is optically thick to X-rays, i.e. $\tau_\lambda > 1$. Emission is not expected to be seen at radii much below this surface if opacity remains high. At first glance, it seems that the formation regions are very distant from the photosphere, ranging between ≈ 10 to $\approx 1000 R_*$. However, there also seems to exist a clear correlation between the $\tau_\lambda = 1$ surface and the formation radii (or onset radii), especially for the S XV and Si XIII ions. The results imply that we see the X-rays emerging from the minimum visible radii, whereas X-rays formed below the $\tau_\lambda = 1$ surface are absorbed. Therefore, although the obtained formation radii are very large, the results may actually

imply that the formation regions of X-rays originating in these ions is much deeper—otherwise, there is no reason to expect a clear correlation between the $\tau_\lambda = 1$ and the formation radii. These results are also consistent with a formation radius of ≥ 600 stellar radii from the N VI lines seen with *XMM-Newton*-RGS (Oskinova et al. 2012).

4.2. Line Profile Modeling Using NLTE Stellar Wind Opacity

The same PoWR wind model as used to evaluate He-like line ratios (see Section 4.1) was used to model emission line profiles using the detailed information about the opacity for X-rays in the cool wind of WR 6. The model provides the wind ionization structure and opacity as a function of radius, and hence the wind radial optical depth in the X-ray band. In this model, the ionization structure (and consequently the mass-absorption coefficient) changes drastically with radius. In particular, helium recombines from double to single ionization at about $45 R_*$.

It is well established that the winds of WR stars are clumped (e.g. Lépine & Moffat 1999). Therefore, to compute the X-ray emission line profiles, we used a 2.5 D stochastic wind model (see the full description in Oskinova, Feldmeier & Hamann 2004, 2006). For simplicity, we assumed an idealized case of spherical clumps as well as a constant filling factor (i.e. the case of $q = 0$ of Equation 1). The wind opacity and velocity law are provided by PoWR models. These models are determined by the UV/optical spectra and are completely independent of the X-ray spectra. With no additional free parameters, we obtained a line profile fully consistent with our asymptotic solution of Equation 1, and justifies the assumptions made in the analytic profile fits, and further supports the fact that X-rays are generated at large radii, outside the acceleration zone.

If we were to assume that X-rays were only from wind shocks in the wind acceleration zone—as in O stars—but which in WR 6 occurs at radii where $\tau \gg 1$, then we would be seeing a very small fraction of the total intrinsic X-ray flux produced—wind models indicate that the optical depth of the wind for X-rays is $\tau \geq 10$. The emergent X-rays have about 10^{-5} of the wind kinetic power ($\frac{1}{2}\dot{M} v_\infty^2$). If the X-rays were all produced in the acceleration zone (below $\sim 30 R_*$), then we would need all or more of the mechanical energy to be converted into X-rays to obtain what we see emerging from optical depths > 10 .

The quantitative models show that plasma responsible for the emergent X-ray line emission is distributed over the large range of radii between ~ 30 – $500 R_*$. The He-like lines also show rather directly that emission is not coming solely from deep in the wind.

4.3. Possible Reason for Extended Emission in Dense Winds

At first glance, it might seem surprising that these winds produce X-rays at much larger radii than seen in winds of single OB stars, as the latter generally form their X-rays not too distant from the wind acceleration zone where the instability is active (Krtićka et al. 2009).

A much denser wind has a higher kinetic energy flux from which to generate X-rays in shocks, and also has locally higher emission measures at all radii. Such a wind also has an overall higher radiative cooling rate as a result of a higher density, so X-ray generation should generally compete more effectively against the adiabatic cooling of expansion. Thus it would be possible for the X-rays from these winds to suffer a kind of “embarrassment of riches,” were it not for wind absorption.

Thus we may simply be seeing the effects of how higher density winds shift their emission to regions where the densities are somewhat comparable to observable X-ray generation in the winds of OB stars. It is not obvious that a completely new mechanism is required, although the hardness of the X-rays from WR 6 remains a puzzle, given that the wind velocity is characteristic of OB stars as well. All this suggests that if we are to look for a unified X-ray generation mechanism in OB and W-R stars, it will need to be an extended emission process that only exhibits its harder and larger-radius components if the densities are high enough for radiative cooling to compete successfully against expansion cooling at such radii.

4.4. X-ray and Optical Variability

It has only recently become known (mainly due to the absence of adequate data) that the intrinsic X-ray emission arising in the winds of single hot stars is subject to slow variability of low amplitude of typically a few percent. Such can be seen in O-type stars ζ Oph, ζ Pup, ξ Per, ζ Ori, and λ Cep (Oskinova, Clarke & Pollock 2001; Nazé, Oskinova & Gosset 2013; Massa et al. 2014; Pollock & Guainazzi 2014; Rauw et al. 2015). The 2010 *XMM-Newton* campaign on WR 6 (Ignace et al. 2013) revealed similar behavior of somewhat larger amplitude over days and weeks, adding to the historical record in which the first set of short X-ray observations that were made with the *Einstein* Observatory between 1979 and 1981 varied in count rate by about a factor of 3 (Pollock 1987). The long *Chandra* observation of WR 6 is ideal for investigating X-ray variability. While the overall count rate changed by about 13% over the observing period, none of the X-ray fluctuations seen appear to be obviously related to the 3.7650 day period of rather variable character seen at longer wavelengths.

During the 2013 *Chandra* campaign, judged by the overall count rates in the dispersed and zeroth-order data, the mean intensity of WR 6 increased by 9% between May and August and

by a further 4% over the 3-day gap between the two final *Chandra* observations. These were similar in scope to the variations seen in the *XMM-Newton* campaign 3 years earlier. With the high count rates detected with the *XMM-Newton*-Newton EPIC instruments, which exceed those of the *Chandra* instruments by factors of more than 30, it was possible to study in detail shorter-term variability within an observation to show the smooth changes that occurred over several hours. We have performed a similar analysis with the *Chandra* data.

The X-ray light curves are shown in Figure 8 and display the same type of slow evolution detected with higher precision with *XMM-Newton*. At its *Chandra* maximum at the beginning of the final *Chandra* observation, WR 6 was at the same brightness within the errors as the maximum observed at the beginning of the *XMM-Newton* campaign in 2010. We did not detect any chromatic component to the variability of the high-resolution spectra; we formed hardness ratio light curves using the first order dispersed photons between the 1.7–8.0 Å “hard” and 8.0–17.0 Å “soft” bands, with null results for variability, within the uncertainties. We also searched for spectral and line variability in somewhat coarser bins than the light curves (28 ks), with null results within the statistics.

Hence, we can only conclude that the overall flux is changing slowly, but cannot say whether it is due to changes in X-ray temperature or volume, or if it is due to variable absorption.

The optical light curve is also shown in Figure 8 and presents some of the most densely sampled optical photometry ever obtained of this or any Wolf-Rayet star. WR 6 was rapidly variable in the optical during the X-ray observations including a rapid decline at the beginning of the second observation and coherent structures lasting for many hours up to as long as a day. The X-ray variability was much slower and of higher amplitude and bears no apparent relation to the optical light curve.

4.5. Evidence of Nucleosynthesis

Our spectral model adopted abundances from Asplund et al. (2009) with CNO modified according to the WN type and WR 6 optical and UV models computed with PoWR (Hamann, Gräfener & Liermann 2006). Abundances of a few species with strong lines were left free in the fit to compensate for systematic effects due to using only 4 discrete temperature components and a simplified absorption model (see Appendix A.1 for details). With this model, we found that we had very large residuals for the H- and He-like lines of sodium (Na XI, 10.021, 10.027 Å; Na X, 10.990 (resonance line), 11.066, 11.074 (intercombination lines), and 11.186 (forbidden line)). Re-fitting the relative abundances and model normalization in this spectral region resulted in an overabundance of Na relative to the abundances of Asplund et al. (2009) by a factor of 6.9 (5.4–8.7 90%

confidence region). We cannot explain this through blends of Fe lines, since the many blends of Fe XVIII are formed at about the same temperatures as other lines in the region, Ne IX being the coolest having maximum emissivity near 4 MK, and Mg XII the hottest at 10 MK. We searched for features not in the atomic database by looking at spectra of sharp-lined coronal sources. While there are features observed near 10 Å with no identification in AtomDB, they are weak and not at the right wavelength to mimic Na XI. It would also be an unlikely coincidence to have anomalies precisely at both the H- and He-like Na wavelengths. Hence, we conclude that the lines are due to Na and that the abundance is enhanced. Figure 10 shows our best fit to the region along with spectra without Na and without both Na and Fe.

Identification of Na in stellar X-ray spectra is rare, but not unprecedented. Sanz-Forcada, Maggio & Micela (2003) measured a flux for Na XI in *Chandra*/HETG spectra of AB Dor, a young rapidly rotating, coronally active K-star, but did not identify the line. García-Alvarez et al. (2005) identified Na XI in the same AB Dor spectrum, and also in a *Chandra*/LETGS spectrum of V471 Tau, a rapidly rotating K2 dwarf and white dwarf binary. Huenemoerder et al. (2013) measured Na XI in the RS CVn stars, σ Gem and HR 1099, two late-type coronally active binaries with among the highest fluences collected with the *CXO*/HETGS. Coronally active stars have an advantage in detecting these weak features in that the lines are generally unresolved; the stars are rapidly rotating, but velocities are still below the instrumental resolution, and hence have relatively high contrast. Abundances in these cases were near solar, to within a factor of two.

We do not know of any instances, however, of Na detection in other hot star wind spectra. Here the broadening of the lines makes such a detection difficult, especially without a deep exposure or enhanced abundances.

We interpret the enhancement of Na as due to nuclear processing—the CNO-cycle can produce Na through the Ne-Na cycle (Cavanna et al. 2014). The amount depends upon the core temperature, and somewhat poorly known nuclear rates (Izzard et al. 2007), but enhancement factors of 6–10 have been predicted by models (Woosley, Langer & Weaver 1995; Chieffi, Limongi & Straniero 1998). The abundances of Ne, Na, Mg, and Al are all related and strongly dependent upon the details of nuclear processing, ultimately determined by the initial mass of the evolving star. The soft X-ray spectrum may be the best place to determine these abundances in WR-stars since the emission mechanisms are relatively simple—no radiative transfer calculations are required in an optically thin plasma. Features of Ne, Mg are strong in the WR 6 spectrum, and Na and Al lines are present. These certainly warrant more careful, detailed analysis to determine their relative abundances since they may provide unique constraints on evolutionary states.

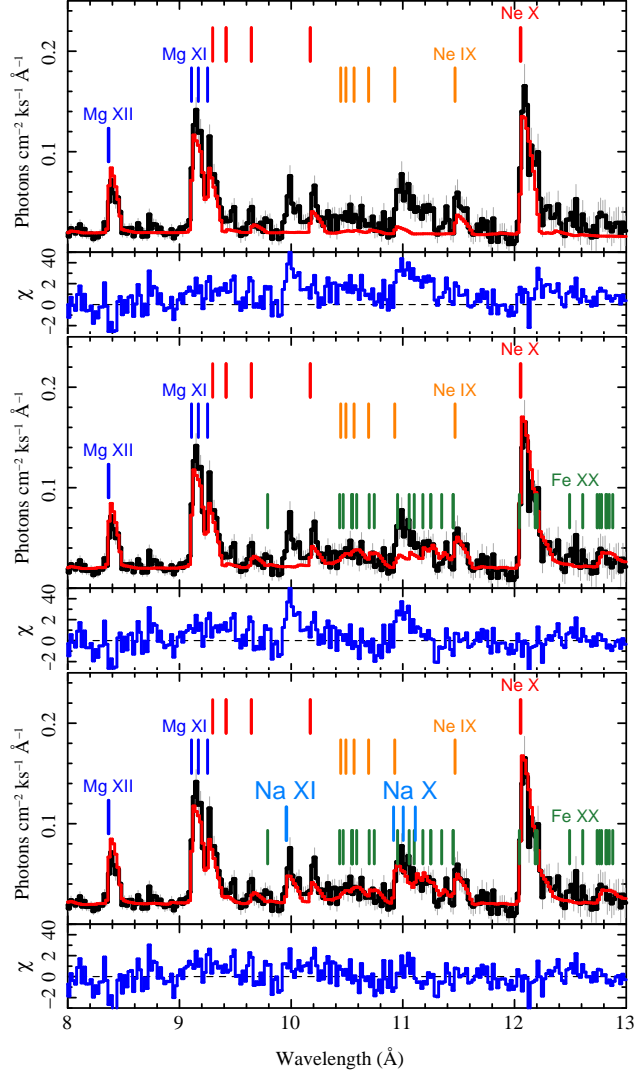


Fig. 10.— The region including the H- and He-like lines of Na XI (10.02 Å) and Na X (10.99 Å). The top panel has both the Na and Fe abundances set to 0.0. In the center panel, we have restored the model’s Fe abundance, and in the lower Na with an abundance 7 times the cosmic value. In each panel the black histogram is the observed spectrum, red is the model, and beneath in blue are the residuals. Series of the brightest lines are marked at their blue edge with a different y -offset for each ion. In the case of Fe, we marked positions of the 30 brightest model lines of Fe XVII–XXIV in the region (all labeled by Fe XX). The reduction of the residuals with the inclusion of Na—at high relative abundance—is clear.

4.6. Fe K Fluorescence

Oskinova et al. (2012) detected Fe K fluorescence in *XMM-Newton* spectra. In our spectra for dispersed or zeroth order, we see no obvious Fe K emission next to the strong Fe XXV emission lines (Figure 2). The fit to the zeroth-order spectrum, however, is slightly improved if we introduce an additional component at 1.94 Å. The fluorescent flux we obtained (3.5×10^{-7} photons $\text{cm}^{-2} \text{s}^{-1}$, with 1σ confidence region of $1.7\text{--}5.4 \times 10^{-7}$ photons $\text{cm}^{-2} \text{s}^{-1}$), is consistent with that measured by Oskinova et al. (2012) in *XMM-Newton* spectra, so the HETGS spectrum is not inconsistent with the prior observations.

The presence of Fe K fluorescence requires hard photons, roughly 7–20 keV, incident on cold Fe (see Drake, Ercolano & Swartz 2008, for example). Hence, we not only have temperatures high enough to produce line emission far out in the wind, there may also be a significant source of fairly hard continuum emission. Our plasma model gives a 7.0–20 keV flux of 6.5×10^{-6} erg $\text{cm}^{-2} \text{s}^{-1}$, implying a yield factor of about 0.05.

Fe K fluorescence is interesting because it can provide constraints on geometry since the amount of fluorescence depends on the hard spectrum and on the relative locations of the cold Fe and hard photons. As such, it has potential to provide another diagnostic of the distribution of hot and cold matter within the wind. The current data, however, are not sufficient to pursue this in detail.

5. Conclusions

Our primary result, based on the resolved line profiles, is that the X-ray emitting wind of WR 6 is undergoing constant spherical expansion, implying a wide separation between the regions from which the X-rays emerge (30–1000 R_*) and the acceleration zone where the line-driven instability is expected to be actively producing shocks ($< 30 R_*$). The sharp blue wings of the X-ray emission line profiles give a good measure of a terminal velocity of $\approx 2000 \text{ km s}^{-1}$, a value within the range of 1700–2500 km s^{-1} determined from UV spectra. These are important conclusions, predicted by the theoretical profiles of Ignace (2001) as very likely in WR star winds with their high continuum opacity. These features could only be realized with a deep exposure with the spectral resolution of *Chandra*/HETG.

The ratios of the He-like lines, in conjunction with the PoWR model atmospheres (under both a simplified single radius of formation or an onset radius with distributed emission) require that the X-rays be produced very far out in the wind, tens to many hundreds of stellar radii. These locations, based on lack of photo-destruction of forbidden lines, are consistent with the line shapes which indicate asymptotic flow, and also with the line shape predictions derived from the detailed

opacity distribution of the PoWR models.

The X-rays from WR 6 are subject to continuous low-level variability on different time scales. It has not yet been possible to properly quantify this variability given its slow and seemingly stochastic behavior, though during observations of a day or more, changes of a few percent have been typical. Neither the optical nor the X-ray variations appear correlated with the known period of 3.765 d, nor are they correlated with each other. It will take the greater sensitivity of future X-ray observatories to significantly detect and correlate such small fluctuations.

The abundance of sodium is significantly enhanced and is consistent with probable nucleosynthesis scenarios in massive stars. This result is highly important for future, more sensitive high-resolution X-ray spectroscopy, since the X-ray region may be the only place to reliably determine the relative abundances of Ne, Na, Mg, and Al—important elemental cycles in nucleosynthesis—in evolved stars prior to supernovae. Obtaining such spectra should be of great interest to new observatories such as *Astro-H* and *Athena*.

There is probably Fe K fluorescence in the wind. This requires hard photons, which if thermal, implies that “cold” Fe is interspersed with very hot plasma, as could be produced by strong shocks. This hot plasma reaches temperatures far higher—up to 50 MK—than present in the embedded wind shocks of “normal” O-stars, like ζ Pup.

The origin of such hard emission at large radii is puzzling; it may be a result of the way high densities at large radii allow the radiative cooling to compete more efficiently with other loss channels like expansion cooling, allowing hot gas to be seen there in WR-star winds but not OB-star winds.

An optically thick wind is not going to reveal the X-rays emitted from embedded shocks in the acceleration region where the line-driven instability is active: for typical acceleration laws, the wind reaches 90% of terminal velocity within 30 stellar radii, and for WR 6, $\tau \gg 1$ at $30 R_*$ over most of the soft X-ray spectrum. Because radiative cooling is efficient in thick winds (and even expansion cooling acts on the scale of the radius), hot gas formed near the acceleration zone would cool before rising to radii that are optically thin to X-rays. However, higher density winds extend efficient radiative cooling to larger radii, offering us a glimpse of mechanisms we could not otherwise detect at such radii. In the thinner winds of OB-stars, the density-squared weighting of emissivity and the rapid decline of density with radius means that any X-ray flux produced outside the acceleration zone is overwhelmed by the inner wind. In WR 6, we can only see the outer wind.

Overall, the origin of X-rays from the outer wind of WR 6 remains a mystery, but whether we have a new mechanism or a new view of the mechanisms also at work in OB-stars, observations such as this offer a glimpse at the spatially extended tail of the X-ray generating processes in hypersonic winds. It is especially challenging to understand the origin of the hardest X-rays

requiring the strongest shocks, but at least such emission can escape from deeper in the wind. It suggests that some gas is accelerated to significantly faster speeds than the average terminal speed, and these fast streams can persist outside the acceleration zone, perhaps by passing through gaps in the clumpy slower wind.

There are a few other X-ray sources among WR-stars which are also thought to be single, where one can exclusively study the wind in X-rays, as opposed to WR-plus-O or -B binaries with strong colliding wind emission. Skinner et al. (2002b) analyzed *XMM-Newton* low-resolution X-ray spectra of WR 110, and Ignace, Oskinova & Brown (2003) noted similarities among WN-stars WR 1, WR 6, and WR 110 in *XMM-Newton* low-resolution X-ray spectra. Skinner et al. (2010) analyzed about a dozen more WN-stars observed with either *Chandra* or *XMM-Newton*. All these WN stars have thermal spectra, soft and hard components (though WR 1 is weak above 4 keV), and are strongly absorbed. Luminosities are around 10^{32} – 10^{33} erg s⁻¹. Of note are hard components which were not expected and not explained by embedded wind-shock models. Furthermore, the lack of evidence for binary companions strongly excluded colliding wind shocks as an explanation. If we place WR 6 on Figures 9 & 10 in Skinner et al. (2010) (using the WR 6 values of $\log L_x = 32.9$, $\log L_{\text{wind}} = 37.8$, and $\log L_{\text{bol}} = 39.2$), then it lies near WR stars 2, 110, and 134. In other words, WR 6 is not unusual in global properties compared to other putatively single WN-type WR stars.

The X-ray spectra for all these other stars, however, are of low resolution. Only high resolution spectra will show whether these other stars share similar wind structure with WR 6 in having X-rays — both hard and soft — produced in the asymptotic uniform spherical outflow. Additionally, we look forward to high resolution and high sensitivity of future observatories at the higher energies of Fe XXV to probe the high energy processes in the deepest wind layers visible.

Acknowledgements: Support for this work was provided by the National Aeronautics and Space Administration through Chandra Award Numbers GO3-14003A and GO5-16009A to MIT (DPH), GO3-14003D to ETSU (RI), GO3-14003B to SAO (JN), and GO3-13003C to UI (KGG), issued by the Chandra X-ray Observatory Center, which is operated by the Smithsonian Astrophysical Observatory for and on behalf of the National Aeronautics Space Administration under contract NAS8-03060. JSN is grateful for support from the Chandra X-ray Center NASA Contract NAS8-03060. LO thanks the DLR grant 50 OR 1302.

We thank Adam Foster and Randall Smith for permission and help in running APEC for a reduced-hydrogen plasma. We also thank Jennifer Lauer for technical and interpretive support concerning variability.

Facilities: CXO (HETG/ACIS)

REFERENCES

- Asplund, M., Grevesse, N., Sauval, A. J., & Scott, P., 2009, *ARA&A*, 47, 481
- Babel, J., & Montmerle, T., 1997, *A&A*, 323, 121
- Baum, E., Hamann, W.-R., Koesterke, L., & Wessolowski, U., 1992, *A&A*, 266, 402
- Blumenthal, G. R., Drake, G. W. F., & Tucker, W. H., 1972, *ApJ*, 172, 205
- Canizares, C. R., et al., 2005, *PASP*, 117, 1144
- Cassinelli, J. P., Miller, N. A., Waldron, W. L., MacFarlane, J. J., & Cohen, D. H., 2001, *ApJ*, 554, L55
- Castor, J. I., Abbott, D. C., & Klein, R. I., 1975, *ApJ*, 195, 157
- Cavanna, F., et al., 2014, *European Physical Journal A*, 50, 179
- Chieffi, A., Limongi, M., & Straniero, O., 1998, *ApJ*, 502, 737
- Cohen, D. H., Li, Z., Gayley, K. G., Owocki, S. P., Sundqvist, J. O., Petit, V., & Leutenegger, M. A., 2014a, *MNRAS*, 444, 3729
- Cohen, D. H., Wollman, E. E., Leutenegger, M. A., Sundqvist, J. O., Fullerton, A. W., Zsargó, J., & Owocki, S. P., 2014b, *MNRAS*, 439, 908
- Crowther, P. A., & Hadfield, L. J., 2006, *A&A*, 449, 711
- Davis, J. E., 2001, *ApJ*, 548, 1010
- de la Chevrotière, A., St-Louis, N., Moffat, A. F. J., & the MiMeS Collaboration 2013, *ApJ*, 764, 171
- Dougherty, S. M., & Williams, P. M., 2000, *MNRAS*, 319, 1005
- Drake, J. J., Ercolano, B., & Swartz, D. A., 2008, *ApJ*, 678, 385
- Feldmeier, A., Puls, J., & Pauldrach, A. W. A., 1997, *A&A*, 322, 878
- Firmani, C., Koenigsberger, G., Bisiacchi, G. F., Moffat, A. F. J., & Isserstedt, J., 1980, *ApJ*, 239, 607
- Foster, A. R., Ji, L., Smith, R. K., & Brickhouse, N. S., 2012, *ApJ*, 756, 128
- Friend, D. B., & Castor, J. I., 1983, *ApJ*, 272, 259

- Fruscione, A., et al., 2006, in SPIE Conference Series, Vol. 6270
- Gabriel, A. H., & Jordan, C., 1969, MNRAS, 145, 241
- Gagné, M., Oksala, M. E., Cohen, D. H., Tonnesen, S. K., ud-Doula, A., Owocki, S. P., Townsend, R. H. D., & MacFarlane, J. J., 2005, ApJ, 628, 986
- García-Alvarez, D., Drake, J. J., Lin, L., Kashyap, V. L., & Ball, B., 2005, ApJ, 621, 1009
- Gayley, K. G., & Owocki, S. P., 1995, ApJ, 446, 801
- Georgiev, L. N., Koenigsberger, G., Ivanov, M. M., St.-Louis, N., & Cardona, O., 1999, A&A, 347, 583
- Gräfener, G., & Hamann, W.-R., 2008, A&A, 482, 945
- Gräfener, G., Koesterke, L., & Hamann, W., 2002, A&A, 387, 244
- Güdel, M., & Nazé, Y., 2009, A&A Rev., 17, 309
- Hamann, W., & Koesterke, L., 1998a, A&A, 333, 251
- Hamann, W.-R., & Gräfener, G., 2004, A&A, 427, 697
- Hamann, W.-R., Gräfener, G., & Liermann, A., 2006, A&A, 457, 1015
- Hamann, W.-R., & Koesterke, L., 1998b, A&A, 333, 251
- Henley, D. B., Stevens, I. R., & Pittard, J. M., 2003, MNRAS, 346, 773
- Hervé, A., Rauw, G., & Nazé, Y., 2013, A&A, 551, A83
- Hervé, A., Rauw, G., Nazé, Y., & Foster, A., 2012, ApJ, 748, 89
- Hillier, D. J., & Miller, D. L., 1998, ApJ, 496, 407
- Howarth, I. D., & Schmutz, W., 1995, A&A, 294, 529
- Huenemoerder, D. P., Phillips, K. J. H., Sylwester, J., & Sylwester, B., 2013, ApJ, 768, 135
- Ignace, R., 2001, ApJ, 549, L119
- Ignace, R., 2015, Advances in Space Research, 56, (submitted)
- Ignace, R., & Gayley, K. G., 2002, ApJ, 568, 954

- Ignace, R., Gayley, K. G., Hamann, W.-R., Huenemoerder, D. P., Oskinova, L. M., Pollock, A. M. T., & McFall, M., 2013, *ApJ*, 775, 29
- Ignace, R., & Oskinova, L. M., 1999, *A&A*, 348, L45
- Ignace, R., Oskinova, L. M., & Brown, J. C., 2003, *A&A*, 408, 353
- Izzard, R. G., Lugaro, M., Karakas, A. I., Iliadis, C., & van Raai, M., 2007, *A&A*, 466, 641
- Kahn, S. M., Leutenegger, M. A., Cottam, J., Rauw, G., Vreux, J.-M., den Boggende, A. J. F., Mewe, R., & Güdel, M., 2001, *A&A*, 365, L312
- Krtićka, J., Feldmeier, A., Oskinova, L. M., Kubát, J., & Hamann, W.-R., 2009, *A&A*, 508, 841
- Lamontagne, R., Moffat, A. F. J., & Lamarre, A., 1986, *AJ*, 91, 925
- Langer, N., 2012, *ARA&A*, 50, 107
- Lépine, S., & Moffat, A. F. J., 1999, *ApJ*, 514, 909
- Leutenegger, M. A., Cohen, D. H., Sundqvist, J. O., & Owocki, S. P., 2013, *ApJ*, 770, 80
- Leutenegger, M. A., Owocki, S. P., Kahn, S. M., & Paerels, F. B. S., 2007, *ApJ*, 659, 642
- Leutenegger, M. A., Paerels, F. B. S., Kahn, S. M., & Cohen, D. H., 2006, *ApJ*, 650, 1096
- Lucy, L. B., & White, R. L., 1980, *ApJ*, 241, 300
- Luo, D., McCray, R., & Mac Low, M., 1990, *ApJ*, 362, 267
- MacFarlane, J. J., Cassinelli, J. P., Welsh, B. Y., Vedder, P. W., Vallergera, J. V., & Waldron, W. L., 1991, *ApJ*, 380, 564
- Massa, D., Oskinova, L., Fullerton, A. W., Prinja, R. K., Bohlender, D. A., Morrison, N. D., Blake, M., & Pych, W., 2014, *MNRAS*, 441, 2173
- Morel, T., St-Louis, N., & Marchenko, S. V., 1997, *ApJ*, 482, 470
- Nazé, Y., Oskinova, L. M., & Gosset, E., 2013, *ApJ*, 763, 143
- Nichols, J. S., & et. al 2015, *ApJ*, 000, 000
- Nichols, J. S., Henden, A. A., Huenemoerder, D. P., Lauer, J. L., Martin, E., Morgan, D. L., & Sundheim, B. A., 2010, *ApJS*, 188, 473
- Oskinova, L. M., 2005, *MNRAS*, 361, 679

- Oskinova, L. M., Clarke, D., & Pollock, A. M. T., 2001, *A&A*, 378, L21
- Oskinova, L. M., Feldmeier, A., & Hamann, W.-R., 2004, *A&A*, 422, 675
- Oskinova, L. M., Feldmeier, A., & Hamann, W.-R., 2006, *MNRAS*, 372, 313
- Oskinova, L. M., Gayley, K. G., Hamann, W.-R., Huenemoerder, D. P., Ignace, R., & Pollock, A. M. T., 2012, *ApJ*, 747, L25
- Oskinova, L. M., Hamann, W., & Feldmeier, A., 2007, *A&A*, 476, 1331
- Owocki, S. P., Castor, J. I., & Rybicki, G. B., 1988, *ApJ*, 335, 914
- Owocki, S. P., & Cohen, D. H., 2001, *ApJ*, 559, 1108
- Parkin, E. R., Pittard, J. M., Nazé, Y., & Blomme, R., 2014, *A&A*, 570, A10
- Pauldrach, A., Puls, J., & Kudritzki, R. P., 1986, *A&A*, 164, 86
- Pollock, A., & Guainazzi, M., 2014, in *The X-ray Universe 2014*, 302
- Pollock, A. M. T., 1987, *ApJ*, 320, 283
- Porquet, D., Mewe, R., Dubau, J., Raassen, A. J. J., & Kaastra, J. S., 2001, *A&A*, 376, 1113
- Rauw, G., et al., 2015, *ArXiv e-prints*
- Robert, C., et al., 1992, *ApJ*, 397, 277
- Sanz-Forcada, J., Maggio, A., & Micela, G., 2003, *A&A*, 408, 1087
- Shenar, T., et al., 2015a, *ArXiv e-prints* (arXiv:1503.03476)
- Shenar, T., et al., 2015b, *ApJ*, (in press)
- Skinner, S. L., Zhekov, S. A., Güdel, M., & Schmutz, W., 2002a, *ApJ*, 579, 764
- Skinner, S. L., Zhekov, S. A., Güdel, M., & Schmutz, W., 2002b, *ApJ*, 572, 477
- Skinner, S. L., Zhekov, S. A., Güdel, M., Schmutz, W., & Sokal, K. R., 2010, *AJ*, 139, 825
- Smith, R. K., Brickhouse, N. S., Liedahl, D. A., & Raymond, J. C., 2001, *ApJ*, 556, L91
- Stevens, I. R., Blondin, J. M., & Pollock, A. M. T., 1992, *ApJ*, 386, 265
- van der Hucht, K. A., 2001, *New A Rev.*, 45, 135

Waldron, W. L., & Cassinelli, J. P., 2001, *ApJ*, 548, L45

Waldron, W. L., & Cassinelli, J. P., 2007, *ApJ*, 668, 456

Woosley, S. E., Langer, N., & Weaver, T. A., 1995, *ApJ*, 448, 315

A. Supplemental Material

A.1. Plasma Model Details

Figure 12 shows the result of a simultaneous fit of the WR 6 spectra over all instruments. The model was a 4-temperature AtomDB (Smith et al. 2001; Foster et al. 2012) plasma with free temperatures and normalizations, and a few free abundances (Ne, Mg, Si, S, and Fe). The model also included a wind absorption component (using wind abundances), absorption from ionized C, N, and O (C V, N IV, O IV, O V; though the oxygen and carbon abundances are very small), and foreground interstellar absorption. The AtomDB model was from a custom run of APEC to provide a model without hydrogen, since this is a WN star, and otherwise using abundances (scaled to mass fractions for a low-H atmosphere) of Asplund et al. (2009), with modifications to CNO for a WN star. The same reduced H and CNO abundances were used for the local (neutral and ionized wind) absorption models.

The model parameters are given in Table 6–8. The foreground absorption value adopted was that used by Oskinova et al. (2012), but which they did not quote. It is less than half that used by Skinner et al. (2002a), but this is reasonable since they only used a single absorption component for both foreground and intrinsic components, whereas we include an intrinsic wind-absorption component. The absorption components are shown in Figure 11.

The fit function is effectively defined as

$$\text{Aped}_4 * \text{windabs} * \text{vphabs_noh} * \text{phabs}$$

where the components implemented in ISIS⁵ are as follows:

`Aped_4` is a 4-component APEC model using our customized low-H database;

`windabs` is a wrapper on the XSPEC edge model to provide local wind absorption by ionized CNO ions (though only N IV is significant);

`vphabs_noh` is a wrapper on the XSPEC to adjust the model to remove hydrogen, for the wind neutral absorption function;

`phabs` is the unmodified XSPEC interstellar absorption function.

⁵See <http://space.mit.edu/cxc/isis>.

In our APEC model, we also used some modifiers to implement photoexcitation of He-like lines⁶ and to apply the line profile model to all lines.

Abundances for Na and Al were done by fitting localized regions, as described in Section 4.5 for Na.

A.2. Calibration of Photon Flux HETG Spectra

A Photon flux spectrum is an approximation to the intrinsic flux and is obtained by dividing the counts spectrum by the model counts for a constant flux spectrum. It incorporates contributions to each wavelength bin from neighboring bins as dictated by the response matrix. Hence, the calibration is better for near-diagonal matrices, such as those for grating spectrometers. Flux calibration can be useful for visualization of a model-independent source intrinsic flux. It does not entail any deconvolution, so the instrumental blur is still included in the photon flux spectrum. If lines are resolved, however, the photon flux will approximate the *unconvolved* model. We do not use photon flux spectra for quantitative analysis, but use forward-folding methods to properly account for spectral features in the response.

See the ISIS manual for a detailed definition, (<http://space.mit.edu/cxc/isis/manual.html>), in particular equations 7.4–7.8.

⁶The He-like database and modifier as implemented in ISIS are available from http://space.mit.edu/cxc/analysis/he_modifier

Table 6 Plasma Model Components

| Temperature [MK] | Emission Measure [10^{54} cm^{-3}] |
|---------------------|---|
| 1.5 | 128 |
| 4.0 | 42 |
| 8.0 | 24 |
| 50.1 | 11 |

Table 7 Plasma Model Abundances

| Element | Fraction ^a | Factor ^b |
|---------|-----------------------|---------------------|
| H | -4.60 | 10^{-4} |
| He | -0.01 | 1.00 |
| C | -4.01 | 0.04 |
| N | -1.82 | 22.80 |
| O | -4.01 | 0.02 |
| Ne | -3.09 | 0.68 |
| Na | -3.71 | 7.00 |
| Mg | -3.32 | 0.71 |
| Al | -4.05 | 1.70 |
| Si | -3.09 | 1.28 |
| S | -3.07 | 2.89 |
| Ar | -4.16 | 1.00 |
| K | -5.54 | 1.00 |
| Ca | -4.22 | 1.00 |
| Fe | -3.39 | 0.33 |
| Ni | -4.65 | 0.33 |

^aDecimal log of the mass fraction.

^bThe enhancement factor relative to the abundances of Asplund et al. (2009).

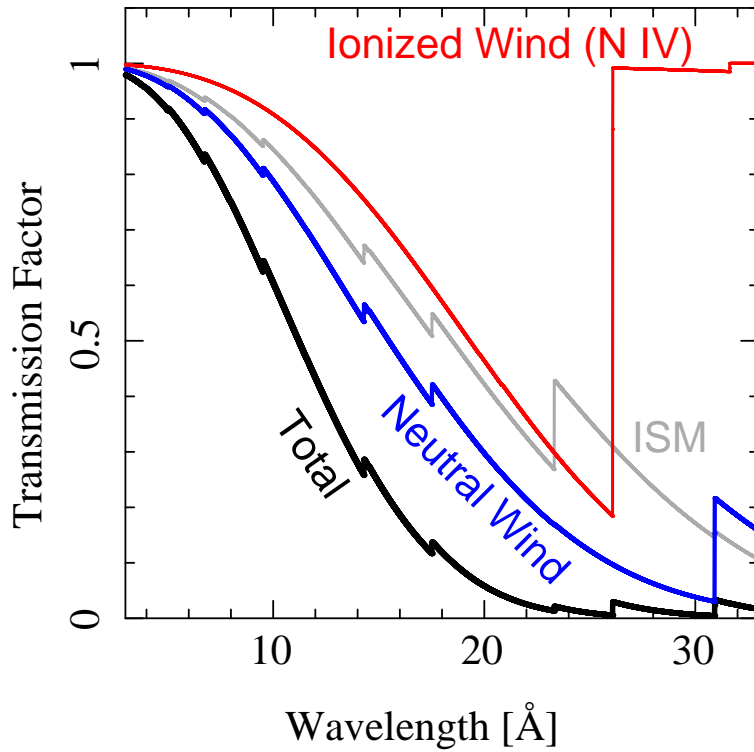


Fig. 11.— The components of the absorption function. The ionized wind is from the XSPEC edge model, the neutral wind is from a modified XSPEC vphabs model, and the ISM is from the XSPEC phabs model. The latter used standard cosmic abundances, while the former used the WR 6 abundances.

Table 8 Absorption Model Parameters

| Component | Scale |
|-----------|-------|
| edge | 0.11 |
| wind | 0.20 |
| ISM | 0.17 |

Note. — The “wind” and “ISM” components used modified XSPEC `vphabs` and `phabs` models, with the hydrogen component scaled out. The parameters are still in the XSPEC units of equivalent hydrogen column density of 10^{22} cm^{-2} . The “edge” model used the XSPEC `edge` function; only N IV 26.085 Å has significant opacity, with an optical depth at threshold of 0.672 per unit scale factor per abundance scale factor.

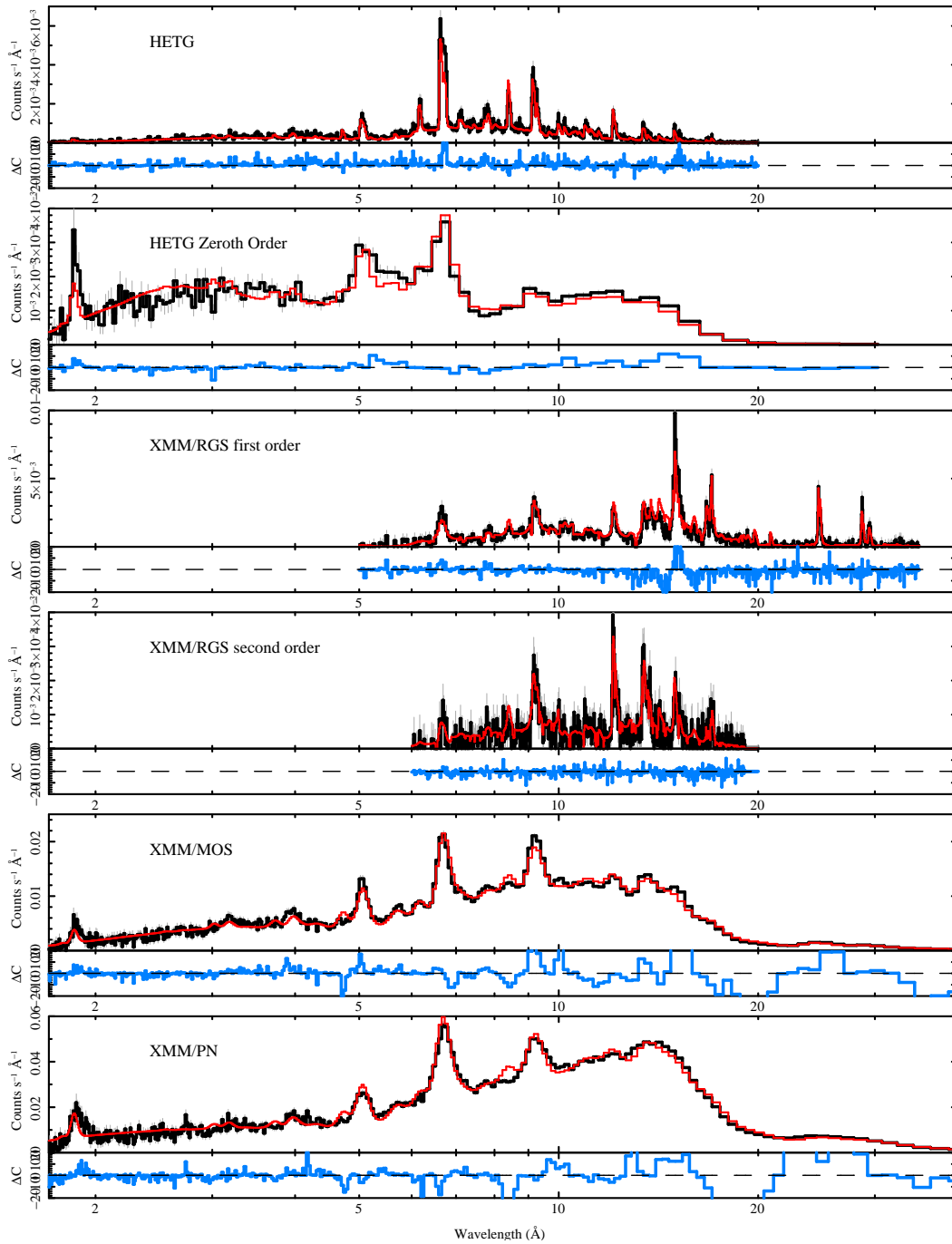


Fig. 12.— Plasma model compared to *Chandra* and *XMM-Newton* spectra. Black histograms are the observed counts, and red are the folded models, which are the same for each case. Below each counts spectrum are residuals.